

Phase-Guided Light Field for Spatial-Depth High Resolution 3D Imaging

Geyou Zhang¹, Ce Zhu¹, Kai Liu², and Yipeng Liu¹

¹ University of Electronic Science and Technology of China

² Sichuan University

Abstract. On 3D imaging, light field cameras typically are of single-shot, and however, they heavily suffer from low spatial resolution and depth accuracy. In this paper, by employing an optical projector to project a group of high-frequency phase-shifted sinusoid patterns, we propose a phase-guided light field algorithm to significantly improve both the spatial and depth resolutions for off-the-shelf light field cameras. First, in order to correct the axial aberrations caused by the main lens of our light field camera, we propose a deformed cone model to calibrate our structured light field system. Second, over wrapped phases computed from patterned images, we propose a stereo matching algorithm, i.e. phase-guided sum of absolute difference, to robustly obtain the correspondence for each pair of neighbored two lenslets. Finally, based on the reference depth by phase-guided stereo matching, we conduct a re-projection and refinement strategy to reconstruct 3D point clouds with spatial-depth high resolution. Experimental results show that, compared with the state-of-the-art active light field methods, the proposed reconstructs 3D point clouds with a spatial resolution of 1280×720 with factors $10 \times$ increased, while maintaining the same high depth resolution and needing merely a single group of high-frequency patterns.

Keywords: Light Field · Structured Light Illumination · 3D Imaging

1 Introduction

Light field cameras captures image from multi-perspective arranged in an array form, thereby boasting a wide depth of field and abundant 3D scene geometry. Light field 3D imaging technologies can be categorized into two types: passive and active. Passive light field 3D imaging is of several noticeable advantages compared to binocular/multiocular 3D imaging, such as no need for hardware synchronization considerations and simpler system configuration. There are primarily four types [9] of passive light field 3D imaging methods: 1) sub-aperture image (SAI) based [10, 18, 20–22, 27], 2) lenslet image based [7, 8, 11, 19], 3) epipolar plane image based [14, 23, 24, 29], and 4) refocused image based [12, 16]. However, passive light field 3D imaging is not capable of high precision industrial inspection due to its limited accuracy.

Active light field 3D imaging, also as known as structured light field (SLF), projects encoded patterns onto the object to achieve high-accuracy 3D reconstruction. SLF is an emerging endeavor for 3D imaging having both the high accuracy of structured light illumination (SLI) and the implicit scene geometry information of light field. Based on the architecture of the commercial hand-held plenoptic camera 1.0 [17], various of researches have explored to significantly improve the accuracy of passive light field 3D imaging by employing active illumination. For SLF calibration, Cai et al proposed a ray calibration [3] and a linear metric model [5] to relate depth values in object space and image space, but an extra auxiliary camera is needed. For 3D reconstruction, multiple-shot phase-shifting fringe patterns [2, 4, 5, 31] are of high accuracy but excessive scanning time consumption, while single-shot sinusoid fringe pattern [1, 6] and speckle pattern [25] can achieve single-shot 3D imaging but sacrifice accuracy.

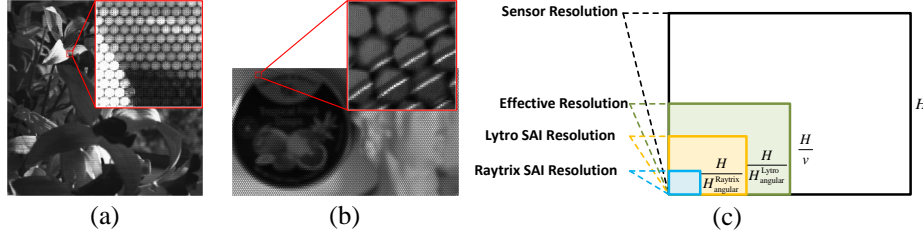


Fig. 1: (a) Raw image of Lytro plenoptic camera 1.0, with 3280×3280 sensor resolution, 9×9 angular resolution, and 364×364 SAI resolution, (b) raw image of Raytrix plenoptic camera 2.0, with 3840×2160 sensor resolution, 35×35 angular resolution, and 110×72 SAI resolution and (c) effective resolution of light field imaging is associated with virtual depth v , which is determined by the number of lenslets that see the same target point along with the vertical or horizontal direction. The existing active light field technology can only obtain depth maps constrained by SAI resolution, far from accomplishing the effective resolution of a plenoptic camera.

The existing active light field techniques employ plenoptic camera 1.0 with a low angular resolution of a few to a dozen pixels and a high SAI resolution (size of sub-aperture image) of hundreds of pixels, as shown in Fig. 1(a), resulting in a considerable resolution of depth map (filled with yellow in Fig. 1(c)), but they failed to achieve the theoretical effective resolution (filled with green in Fig. 1(c)) of light field imaging. As a commercial-grade camera, the plenoptic camera 1.0 is not suitable for industrial conditions and has already stopped production. Different from plenoptic 1.0, in 2012, Raytrix company developed industrial-grade plenoptic camera 2.0 with an improved angular resolution to dozens of pixels, as shown in Fig. 1(b), and currently has dominated the majority of the light field camera market share. The following problem is that, if the active light field algorithms tailored for plenoptic camera 1.0 are directly migrated to plenoptic camera 2.0, the loss of depth map resolution will become very serious

due to the low SAI resolution (filled with blue in Fig. 1(c)) of plenoptic camera 2.0.

To sum up, we notice that the active light field techniques commonly suffer from the constraint of SAI resolution, preventing the depth resolution from achieving the effective resolution, this problem has become more severe in the current plenoptic camera 2.0. Consequently, the application of active light field technique in precision industrial inspection is hindered by the loss of depth map spatial resolution. Consequently, a natural question emerges: **How** can we eliminate the resolution constraint on the depth map in active light field 3D imaging?

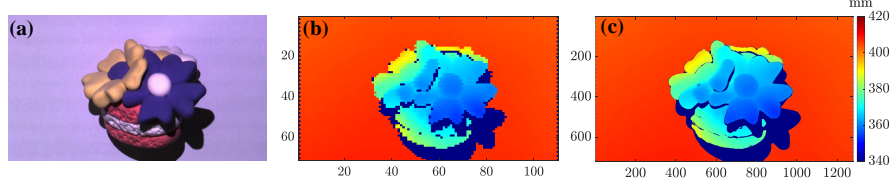


Fig. 2: (a) Measured object, (b) state-of-the-art active light fields [2, 4, 5] employ SAI array resulting in low spatial resolution depth map (resolution: 110×71), and (c) our PGLF works on lenslet image array to have high spatial resolution depth map (resolution: 1280×720).

To address this, in this paper, we present a phase-guided light field (PGLF) 3D imaging pipeline for plenoptic camera 2.0 architecture, the spatial resolution of the depth map is improved by a factor of $10 \times$ compared with state-of-the-art active light field techniques as shown in Fig. 2. Moreover, by leveraging the implicit 3D scene geometry of light field images, the high-frequency ambiguity of the wrapped phase can be eliminated, thereby achieving unambiguous 3D reconstruction from only a single group of high-frequency patterns, thus significantly reducing scanning time consumption.

2 Contributions

In the existing passive and active light field techniques, the depth map resolution is limited by the SAI resolution. Our method breaks this limitation and improves the depth map resolution up to the optical effective resolution [19] of the plenoptic camera. Our method is tailored for plenoptic camera 2.0 with high angular resolution, for instance, consider a Raytrix R8 plenoptic camera with an angular resolution of 35×35 and spatial resolution of 110×71 , i.e., a sensor resolution of 3840×2160 , on the measurement circumstance with a virtual depth of approximately 3, if we ignore the defocus of the micro-lens, theoretically, our method accomplishes an effective resolution ratio [19] (ERR, the ratio of effective resolution and sensor resolution) of $1/3$ and achieves 3D imaging with a resolution of 1280×720 , while previous SLF methods is of the ERR of $1/35$ and can merely achieve 3D imaging with a resolution of 110×71 .

To the best of our knowledge, we are the first to relieve the limitation on depth map resolution constrained by SAI resolution in active light field imaging. Our method enables the plenoptic camera 2.0 to approach its optical limitation for 3D imaging, resulting in a $10\times$ enhancement in the resolution of depth images when compared to existing active and passive light field 3D imaging techniques. This improvement empowers light field 3D imaging for dense and precise 3D measurements, such as defect detection and reverse engineering. Moreover, by exploiting the reference depth map generated by our PGLF algorithm, only one group of fringe is needed for 3D reconstruction, thereby significantly reducing time consumption by half. In applications such as automatic optical inspection, this efficiency gain translates into considerable time savings.

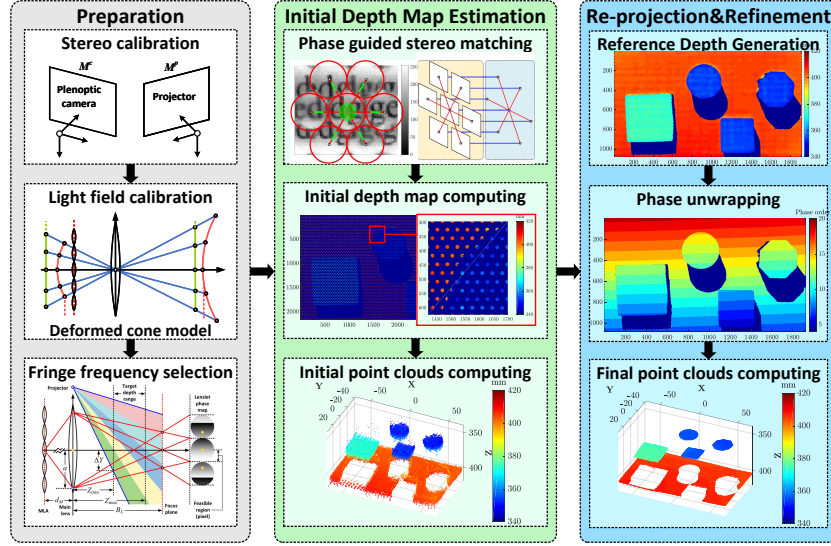


Fig. 3: Flowchart of our method (gray box: calibrate structure light field system with our DCM, green box: initial depth map by phase-guided light field, and blue box: re-projection and refinement strategy for dual-high resolution).

The procedure of our method is shown in Fig. 3, which clarifies that the main contributions of this paper are:

- SLF system calibration procedure with a deformed cone model (DCM) to address axial aberration issue.
- Phase-guided sum of absolute difference (PSAD) cost to robustly achieve stereo matching between adjacent lenslet images.
- Re-projection and refinement strategy for generating spatial-depth high resolution 3D point clouds.

3 Preparation for SLF 3D Imaging

Passive light field is challenged by weak texture and depth discontinuity issues. To tackle these problems, we adopt an active stereo strategy and project at least 3 phase-shifting fringe patterns as $I_n^p(x^p, y^p) = \frac{1}{2} + \frac{1}{2} \cos\left(\frac{2\pi f y^p}{H^p} - \frac{2\pi n}{N}\right)$, where, (x^p, y^p) is the coordinate in the projector space, the term I_n^p is the grayscale intensity of the pixel, the integer-valued f is the spatial frequency of the fringes, H^p is the height of the projector's spatial resolution in rows, and n and N are the index and total number of the phase shifts. Then the wrapped phase can be computed as

$$\phi = \tan^{-1} \left[\frac{\sum_{n=0}^{N-1} I_n^c \sin\left(\frac{2\pi n}{N}\right)}{\sum_{n=0}^{N-1} I_n^c \cos\left(\frac{2\pi n}{N}\right)} \right], \quad (1)$$

Our SLF system consists of a plenoptic camera and a projector. Two calibrations need to be performed to comprehensively describe the system: 1) stereo calibration: calibrate the camera-projector pair; 2) light field calibration: calibrate plenoptic camera parameters.

3.1 Stereo Calibration

We create a virtual camera overlapping the position of the plenoptic camera, the resolution is set to the effective resolution of the plenoptic camera under the actual virtual depth. For example, when we use a plenoptic camera that boasts a sensor resolution of 3840×2160 to measure objects with a virtual depth of approximately 3, the virtual camera resolution should be correspondingly set to 1280×720 . The images captured by the virtual camera are rendered from light field images by our phase-guided stereo matching (Section 4.1). Our stereo calibration is for the virtual camera and projector.

The camera-projector pair can be described by perspective projection matrices \mathbf{M}^c and \mathbf{M}^p , which can be solved by least squared method [26]. Once the camera-projector pair is calibrated, the triangulation based 3D reconstruction typically computes point clouds [13] by

$$\begin{bmatrix} X & Y & Z \end{bmatrix}^T = G_0^{-1} h, \quad (2)$$

where G and h are derived from \mathbf{M}^c and \mathbf{M}^p . Note that the world coordinate is established to coincide with the camera coordinate system in our calibration.

3.2 Light field Calibration

An ideal plenoptic camera follows a linear imaging model [7] as

$$Z = \frac{z f_L}{z - f_L}, z = v d_\mu + d, v = \frac{D_\mu}{D_\mu - D} \quad (3)$$

where z is the image distance of the target 3D point (X, Y, Z) , v is the virtual depth, D is the corresponding point distance in the adjacent lenslet images, moreover, prior optical system parameters: d_μ is the distance between the sensor plane and the MLA plane, D_μ is the diameter of each lenslet in pixels, f_L is the focal length of the main lens.

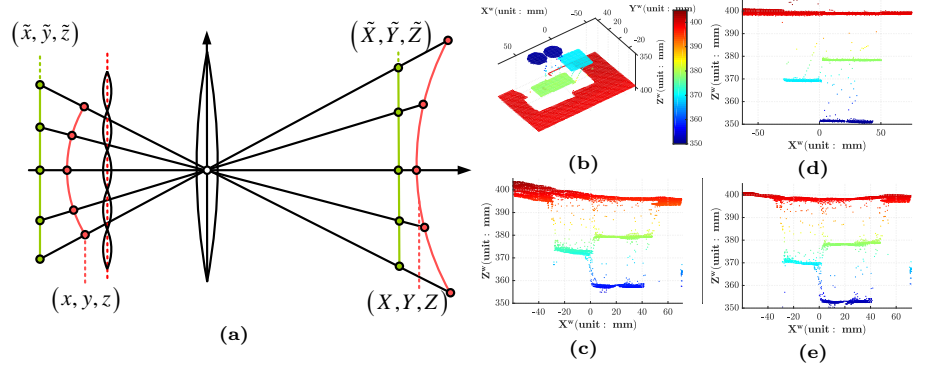


Fig. 4: (a) Our DCM for describing axial aberration. Point clouds of the gypsum blocks: (b), (d) ground truth computed by Eq. (2), (c) linear model (Eq. (2)), and (e) our DCM.

However, the actual optical imaging process suffers from aberrations in the main lens, which causes the depth deformation phenomenon and significantly reduces the accuracy of light field 3D imaging as exemplified in Fig. 4(c). This is primarily attributed to axial aberration: field curvature and astigmatism. Therefore, as demonstrated in Fig. 4(a), assuming that the field curvature and astigmatism are functions of the incident angle of the chief ray (θ_x, θ_y) and the image distance z (equivalent to virtual depth [19] v), we propose a DCM for characterizing the imaging distance \tilde{z} , free from axial aberrations, as a function of (θ_x, θ_y, v) with the aid of parameters \mathbf{a} , k , and d :

$$\tilde{z}(\theta_x, \theta_y, v) = \mathbf{a}^T \mathbf{p} (1 + kv) (vd_\mu + d), \quad (4)$$

where

$$\begin{cases} \mathbf{a} = [1 & a_1 & a_2 & a_3 & a_4 & a_5]^T \\ \mathbf{p} = [1 & \theta_x & \theta_y & \theta_x \theta_y & \theta_x^2 & \theta_y^2] \end{cases}$$

and

$$\begin{bmatrix} \theta_x \\ \theta_y \end{bmatrix} = \frac{1}{Z} \begin{bmatrix} X \\ Y \end{bmatrix} = \frac{1}{z} \begin{bmatrix} x \\ y \end{bmatrix}. \quad (5)$$

To calibrate the parameter \mathbf{a} , we successively scan a plate for M times within the desired depth range. Then we select T lenslet center pixels as the target

points. Therefore, we can numerically solve \mathbf{a} by nonlinear least squared method as

$$[\mathbf{a}, k, d] = \arg \min_{[\mathbf{a}, k, d]} \|\mathbf{z} - \tilde{\mathbf{z}}(\theta_{x,m,t}, \theta_{y,m,t}, v_{m,t})\|, \quad (6)$$

where $\|\cdot\|$ denotes Euclidean norm, \mathbf{z} and $\tilde{\mathbf{z}}$ are vectors computed with $z_{m,t} = Z_{m,t}f_L/(Z_{m,t} - f_L)$ and $\tilde{z}_{m,t} = \tilde{z}(\theta_{x,m,t}, \theta_{y,m,t}, v_{m,t})$ during the M times scanning with T target points each time, respectively, in which $Z_{m,t}$ and $v_{m,t}$ are computed by Eq. (2) and phase-guided stereo matching (we will illustrate in section 4.1), respectively.

By replacing z in Eq. (3) with \tilde{z} , we can effectively compensate the depth warping induced by axial aberration in light field 3D imaging as shown in Fig. 4(d).

3.3 Calibration Procedure

Algorithm 1: SLF system calibration

Input:
 Captured images of LF calibration plates: $\{P_{m,n}\}$.
 Captured images of stereo calibration target: $\{Q_n\}$.
Output:
 Virtual camera and projector matrices: $\mathbf{M}^c, \mathbf{M}^p$.
 Plenoptic camera intrinsics: \mathbf{a}, k, d .

- 1 $\phi^Q \leftarrow \text{ComputePhase}(\{Q_n\})$
- 2 $D^Q \leftarrow \text{LensletPhaseMatching}(\phi^Q)$
- 3 $\{Q_n^r\} \leftarrow \text{Refocus}(\{Q_n\}, D^Q)$
- 4 $\mathbf{M}^c, \mathbf{M}^p \leftarrow \text{StereoCalibration}(\{Q_n^r\})$
- 5 **for** $m \leftarrow 1$ **to** M **do**
- 6 $\phi_m^P \leftarrow \text{ComputePhase}(\{P_{m,n}\})$
- 7 $(\mathbf{X}_m, \mathbf{Y}_m, \mathbf{Z}_m) \leftarrow \text{Compute3DSLl}(\phi_m^P, \mathbf{M}^c, \mathbf{M}^p)$
- 8 $\mathbf{D}_m^P \leftarrow \text{LensletPhaseMatching}(\phi_m^P)$
- 9 $\tilde{\mathbf{z}}_m \leftarrow \tilde{z}(\frac{\mathbf{X}_m}{\mathbf{Z}_m}, \frac{\mathbf{Y}_m}{\mathbf{Z}_m}, \frac{D_\mu}{D_\mu - \mathbf{D}_m^P})$
- 10 $\mathbf{z}_m \leftarrow \frac{\mathbf{Z}_m f_L}{\mathbf{Z}_m - f_L}$
- 11 **end**
- 12 $\mathbf{z} \leftarrow \text{Concat } \mathbf{z}_1, \dots, \mathbf{z}_M$
- 13 $\tilde{\mathbf{z}} \leftarrow \text{Concat } \tilde{\mathbf{z}}_1, \dots, \tilde{\mathbf{z}}_M$
- 14 $[\mathbf{a}, k, d] \leftarrow \arg \min_{[\mathbf{a}, k, d]} \|\mathbf{z} - \tilde{\mathbf{z}}\|$

Note that the phase in the feasible region should be single-valued, which is an indispensable guarantee for stereo matching. Thus, we propose a **uniqueness constraint** for fringe frequency selection. Implementation details can be found in the supplementary material. Our proposed calibration method for SLF system is summarized by Algorithm 1. We list the notations in Algorithm 1:

ComputePhase: Eq. (1), LensletPhaseMatching: Section 4.1, Refocus: Section 5.3, Compute3DSL: Eq. (2), StereoCalibration: Ref. [26], and Concat: Concatenate elements.

4 Initial Depth Map Estimation

Phase can be treated as a robust texture for stereo matching of adjacent lenslet images. Before we conduct the phase-guided stereo matching, to avoid invalid calculations, the feasible region of corresponding point distance $[D_{\min}, D_{\max}]$ and the radius r of the circularly-shaped area to be computed in each lenslet image can be determined according to the desired depth range $[Z_{\min}, Z_{\max}]$, as shown in Fig. 5(b).

4.1 Phase-Guided Stereo Matching on Lenslets

We select six lenslet images circled with the red solid line in Fig. 5(a) for phase-guided stereo matching. Due to the directionality of the phase, we exclude the target lenslets that hold $\frac{\mathbf{g} \cdot \mathbf{u}}{|\mathbf{g}| |\mathbf{u}|} < \cos(\pi/3)$, where the phase gradient $\mathbf{g} = [G_x \ G_y]$, G_x and G_y are the medians of the horizontal and vertical gradient of ϕ within a 7×7 square window centered at the template pixel, \mathbf{u} is the unit vector from the template to target lenslet, from which we ensure the phase gradient maintains a sufficient component along the epipolar.

Different from the stereo matching of grayscale images, we focus on the absolute value rather than the gradient or relative value in phase-based matching. Thus, the sum of absolute differences (SAD) is relatively appropriate among the block-matching methods. However, its accuracy diminishes when the occluder in the lenslet image begins to dominate over non-occluded pixels, resulting in errors at depth discontinuities.

For suppressing the depth discontinuous error, we propose a PSAD algorithm for stereo matching, based on two key assumptions to increase the robustness, 1) **phase adjacency**: in the wrapped phase ϕ , the closer the phase difference between two pixels is to 0 or 2π , the more likely they are to be adjacent in 3D space, and 2) **pixel adjacency**: the closer the distance between two pixels, the more likely they are to be adjacent in 3D space. Consequently, spatial adjacency can be used for weighting the cost function. Moreover, to more precisely describe the spatial adjacency, the phase gradient should be considered. Thus, we model the tangent plane of phase with the gradient information of phase map neighboring the template pixel \mathbf{s}_j^c as

$$\tilde{\phi}(\mathbf{s}^c) = \phi(\mathbf{s}_j^c) + \mathbf{g}_j(\mathbf{s}^c - \mathbf{s}_j^c)^T, \quad (7)$$

where $\mathbf{s}^c = (x^c, y^c)$ denotes a arbitrary 2D index of the phase map ϕ .

Further, the weight of block matching can be given as

$$W(\mathbf{s}^c) = \begin{cases} 1, & W_0(\mathbf{s}^c) \geq \tau_1 \\ 0, & W_0(\mathbf{s}^c) < \tau_1 \end{cases}, \quad (8)$$

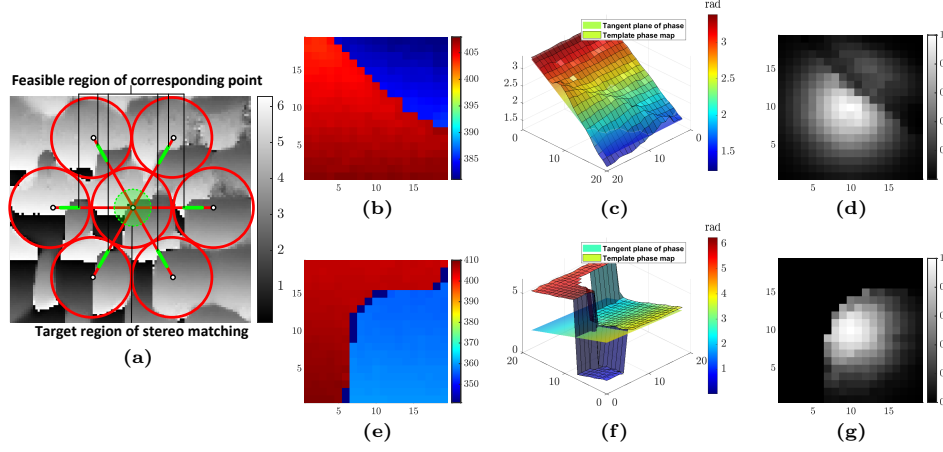


Fig. 5: (a) Diagram of phase-guided stereo matching (phase map of (e), (f), and (g)). (b) and (e) depth, (c) and (f) ϕ and $\tilde{\phi}$, (d) and (g) W_0 , within two lenslet images.

where

$$\begin{cases} W_0(\mathbf{s}^c) = \exp\left(-\frac{\|\mathbf{s}^c - \mathbf{s}_j^c\|}{2\sigma_s^2}\right) \exp\left(-\frac{\Delta\phi^2(\mathbf{s}^c)}{2\sigma_\phi^2}\right) \\ \Delta\phi(\mathbf{s}^c) = \min(\Delta\phi_0(\mathbf{s}^c), |\Delta\phi_0(\mathbf{s}^c) - 2\pi|) \\ \Delta\phi_0(\mathbf{s}^c) = |\tilde{\phi}(\mathbf{s}^c) - \phi(\mathbf{s}^c)| \end{cases},$$

truncation threshold τ_1 is set to 0.4, σ_s is set to $0.5w$, the square window width w is set to 13, and σ_ϕ is set to $3|\mathbf{gu}|$ for adapting to various regions with different phase gradients. The homogeneous pixels of \mathbf{s}_j^c are assigned higher W_0 as depicted in Fig. 5. Finally, the PSAD cost is

$$C(\mathbf{s}_j^c, D) = \sum_{\mathbf{s}^c \in \mathcal{E}} \frac{\min(W(\mathbf{s}^c) \Delta\phi(\mathbf{s}^c, D), \tau_2)}{N_{\mathcal{E}}}, \quad (9)$$

where

$$\begin{cases} \Delta\phi(\mathbf{s}^c, D) = \min(\Delta\phi_0(\mathbf{s}^c, D), |\Delta\phi_0(\mathbf{s}^c, D) - 2\pi|) \\ \Delta\phi_0(\mathbf{s}^c, D) = |\phi(\mathbf{s}^c) - \phi(\mathbf{s}^c + D\mathbf{u})| \end{cases},$$

τ_2 is set to $2|\mathbf{gu}|$, \mathcal{E} is a set of the valid adjacent pixels within a $w \times w$ rectangular window centered at \mathbf{s}_j^c , $N_{\mathcal{E}}$ is the number of elements in \mathcal{E} , and $D \in [D_{\min}, D_{\max}]$. By minimizing $C(\mathbf{s}_j^c, D)$, we can compute the corresponding point distance D . As a result, The depth discontinuous error is effectively suppressed in the stereo matching results (i.e., reference depth map, we will illustrate how to generate it in the subsequent section) as shown in Fig. 6(e)-(g).

After stereo matching, we average the valid corresponding point distances to have D , and put D into Eq. (3), the initial depth Z_r can be computed and shown in Fig. 6(a), which visually presents a regularly distributed speckle pattern.

4.2 Initial 3D Point Clouds Computing

X_r and Y_r are needed to correct the depth deformation with incident angle (θ_x, θ_y) . According to the geometrical optics in a plenoptic camera, we derive the expression as

$$\begin{bmatrix} X_r \\ Y_r \end{bmatrix} = \mathbf{k}Z_r + \mathbf{b}. \quad (10)$$

Implementation details can be found in the supplementary material. Then we compute the incident angle (θ_x, θ_y) by Eq. (5), and subsequently substitute (θ_x, θ_y, v) into Eq. (4) to have corrected depth \tilde{Z}_r . Finally, we compute \tilde{X}_r and \tilde{Y}_r with $(\theta_x, \theta_y, \tilde{Z}_r)$ to have initial 3D point clouds.

5 Re-projection and Refinement Strategy for Accurate Point Clouds

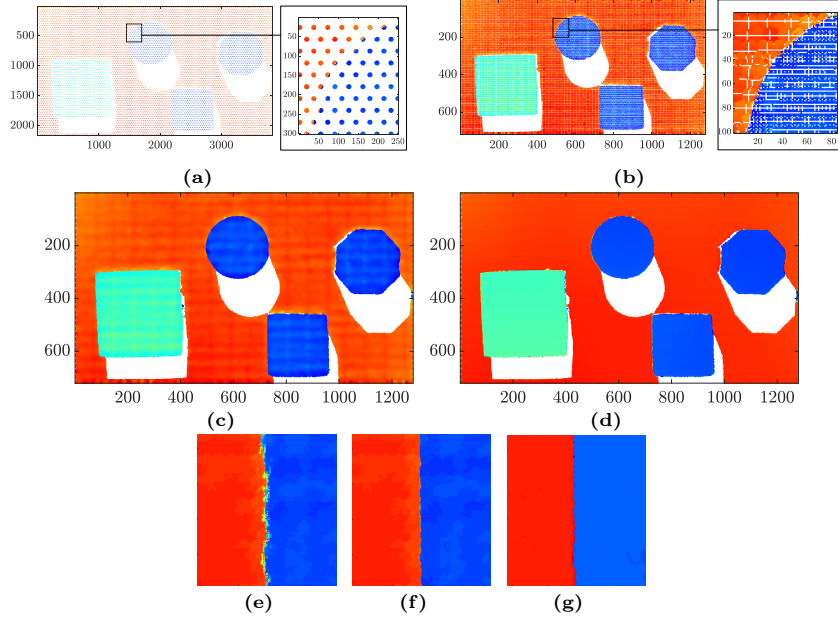


Fig. 6: Re-projection and refinement strategy for accurate point clouds. (a) The initial depth map, (b) re-projected depth map, (c) reference depth map, and (d) final depth map. Our PSAD exhibits more robust performance at leaping area of the depth map: (e) classical SAD, (f) PSAD, and (g) ground truth.

In order to reconstruct accurate point clouds, we propose a re-projection and refinement strategy in this section. First, we generate a reference depth map from

the initial point clouds by re-projection, interpolation, and filtering, as shown in Fig. 6(c); second, we refocus the captured fringe images according to the stereo matching results and compute the wrapped phase; finally, we compute the phase order to unwrap the phase according to the reference depth map, and compute the accurate 3D point clouds with the absolute phase, as shown in Fig. 6(d). Implementation details in this section can be found in the supplementary material.

6 Experimental Results

6.1 Configuration

The proposed algorithm is implemented on an AMD Ryzen 9 7945HX @ 2.50 GHz with 16 GB RAM and written in MATLAB. Our experimental system consists of a Raytrix R8 plenoptic camera with angular resolution of 35×35 and spatial resolution of 110×71 (imaging on a 3840×2160 resolution sensor), and a TI DLP4500 projector with a resolution of 912×1140 . The parameter settings of our algorithm are clarified in section 3.

6.2 Qualitative Evaluations

In the first group of experiments, we employed our method and state-of-the-art active light field techniques to reconstruct several clay handicrafts, thereby comparing the resolving ability of the depth map. The ground truth is obtained by traditional multi-frequency temporal phase shifting profilometry [26]. The results are shown in Fig. 7, our method exhibits clear and sharp depth at discontinuities, while existing methods exhibit a mosaic-like pattern due to their lower spatial resolution. Therefore, our method achieves a stronger resolving ability than existing active light field techniques.

Our method only utilizes a single group of fringe patterns to have the equivalent accuracy as the multiple-shot active light field techniques, while achieving a significantly improved resolution of depth map. A visualized comparison with state-of-the-art active light field methods [2, 4, 5] is demonstrated in the supplementary materials.

6.3 Quantitative Evaluations

In the first set of experiments, we quantitatively evaluate 1) reference depth: the performance of our DCM for suppressing the depth deformation caused by axial aberration; 2) final point clouds: the absolute accuracy of our final result. We employed our method with linear LF imaging model and the proposed DCM to reconstruct several clay handicrafts, with the frequency of $f = 32$ and phase shifting step number of $N = 6$, respectively, and simultaneously obtained the ground truth point cloud with multi-frequency temporal phase shifting profilometry, with the frequency of $f = \{1, 8, 32\}$ and phase shifting step number of $N = \{3, 3, 6\}$. The 3D reconstruction results are presented in Fig. 7 and were analyzed in qualitative evaluation.

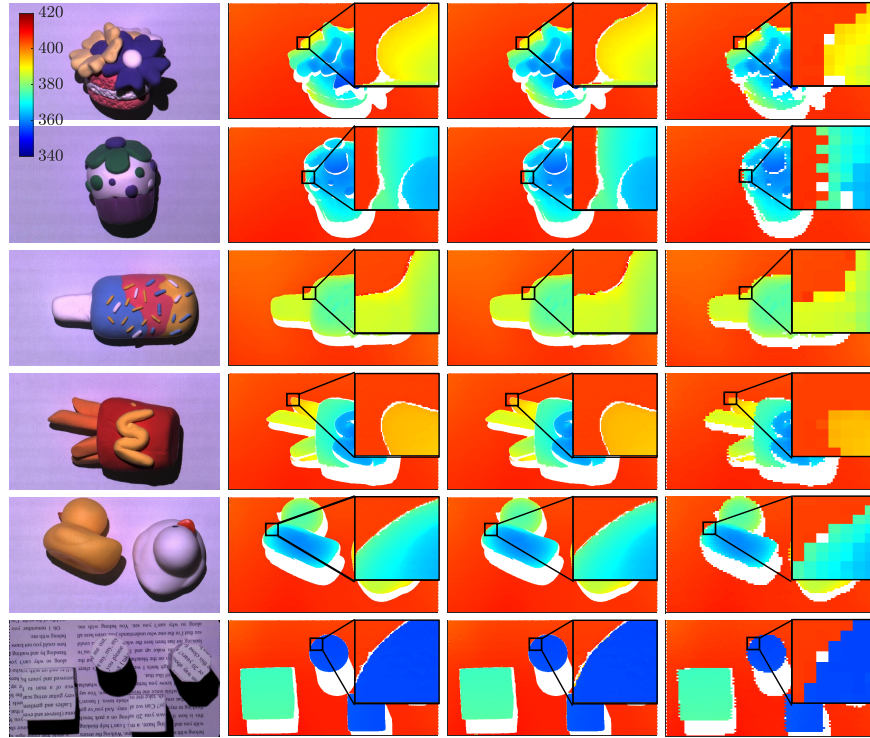


Fig. 7: Visualization of the reconstruction results. **Column 1:** measured object, **Column 2:** ground truth, **Column 3:** our final result (resolution: 1280×720), **Column 4:** state-of-the-art active light field techniques [2, 4, 5] (resolution: 110×71). Our method exhibits clear and sharp depth at discontinuities, while existing methods exhibit a mosaic-like pattern due to their lower spatial resolution. Therefore, our method achieves a stronger resolving ability than existing active light field techniques.

Table 1: Measurement results of handicrafts (units: mm).

no.	Linear LF model			Our DCM		
	Reference depth		SR	Reference depth		SR
	RMSE	MAE		RMSE	MAE	
1	8.158	7.197	81.47%	1.991	1.583	99.61%
2	7.706	6.517	90.12%	1.409	1.094	99.72%
Mean	7.932	6.857	85.80%	1.700	1.339	99.67%

The accuracy of the reference depth map determines the success rate (SR) of phase unwrapping. Therefore, we first to quantitatively assess the accuracy of the reference depth map, we employ the root mean squared error (RMSE) and mean absolute error (MAE) as metrics for evaluating reference depth. We also use the success rate (SR) of unwrapping for the final point clouds as an

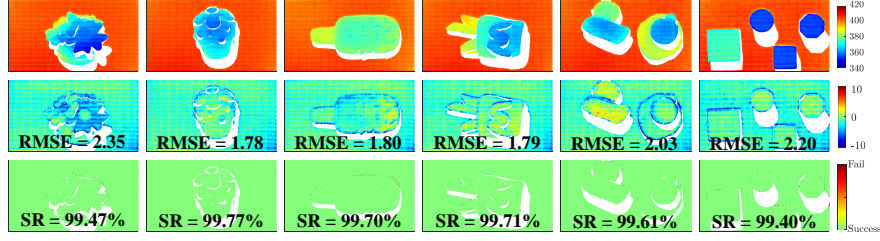


Fig. 8: Visualization of the reconstruction results (resolution: 1280×720). **Row 1:** reference depth obtained in section 5, **Row 2:** error of reference depth (mm), and **Row 3:** SR of unwrapping in final result.

evaluation criterion. The results are shown in Fig. 8. It can be seen that the reference depth is of reliable accuracy to ensure a high SR of phase unwrapping, thereby reducing the outliers in the final point clouds.

Then we slightly adjust the focal distance of the plenoptic camera and measure the clay handicrafts again, the results of the two groups of measurements are listed in Tab. 1. It is evident that when compared with the linear LF imaging model, the error in reference depth obtained by our DCM is significantly reduced in RMSE and MAE, consequently a large area of unwrapping failed region is eliminated, so the SR of unwrapping is improved from 85.80% to 99.67%. We conclude that our DCM can effectively suppress the axial aberration of the main lens of a plenoptic camera. Moreover, our PSAD shows robust performance over depth-discontinuous areas.

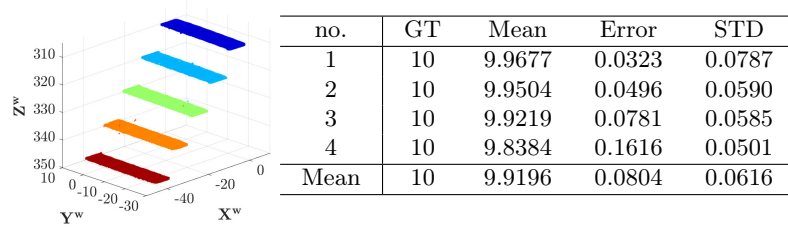


Fig. 9: The measured result of gauge blocks (units: mm).

The second set of experiments aims at assessing the absolute error of our 3D reconstruction method. We conduct the following measurements at a distance of 400 mm: 1) step height measurement: we measure the step height of five gauge blocks arranged in tiers, each with a known ground truth value of 1cm. The results of the measured step height of the staircase are visualized in Fig. 9. 2) circle center distance measurement: we measure a calibration board featuring a grid of 6×7 circular identifiers, and compute the circle center distance according to the measured point cloud. The fringe patterns are of settings $f = 32$ and

$N = 8$. The results are listed in Tab. 2. The experimental results show that,

Table 2: Measurement results of circle center distance (units: mm).

GT	Mean	MAE	STD	Percentage MAE
50	49.9492	0.0508	0.0436	0.1016%

our PGLF accomplishes dual-high measurements on spatial and depth with resolution of 1280×720 and standard derivation of less than $70 \mu\text{m}$. Therefore, we conclude that our method is capable of industrial-grade 3D measurements. It is notable that the MAEs reach 0.0804 mm and 0.0508 mm for measuring step height and circle center distance, respectively. The MAE can primarily be attributed to distortions caused by the main lenses in the plenoptic camera and projector, which can be addressed by well-documented lens distortion correction methods [15, 28, 30].

The proposed algorithm required about 80s for each reconstruction procedure. It is worth noting that this algorithm is implemented using CPU multi-threading (10 threads) in MATLAB without any optimization. Therefore, it is anticipated that a substantial improvement in speed could be achieved by parallelizing stereo matching through GPU utilization.

7 Conclusions and Future Work

In summary, we proposed a PGLF pipeline for reconstructing spatial-depth high resolution and unambiguous 3D point clouds from a merely single group of high-frequency fringe patterns, implemented in mainstream plenoptic camera 2.0 architecture. We conclude that our method’s dual-high resolution enables LF 3D imaging to achieve dense and precise industrial-grade 3D measurements, and the reduction in the number of fringe patterns significantly improves scanning time efficiency.

However, there are several existing issues that warrant future consideration. Although our PSAD effectively overcomes depth-discontinuous issue in most cases, the result is unsatisfactory when the depth difference exactly induce a phase difference of integer multiple periods. Another issue of the proposed is the reliance on graphic process units in practical applications due to the high time consumption.

References

1. Cai, Z., Liu, X., Pedrini, G., Osten, W., Peng, X.: Accurate depth estimation in structured light fields. *Optics Express* **27**(9), 13532–13546 (2019) 2
2. Cai, Z., Liu, X., Pedrini, G., Osten, W., Peng, X.: Structured-light-field 3d imaging without phase unwrapping. *Optics and Lasers in Engineering* **129**, 106047 (2020) 2, 3, 11, 12

3. Cai, Z., Liu, X., Peng, X., Gao, B.Z.: Ray calibration and phase mapping for structured-light-field 3d reconstruction. *Optics Express* **26**(6), 7598–7613 (2018) [2](#)
4. Cai, Z., Liu, X., Peng, X., Yin, Y., Li, A., Wu, J., Gao, B.Z.: Structured light field 3d imaging. *Optics express* **24**(18), 20324–20334 (2016) [2](#), [3](#), [11](#), [12](#)
5. Cai, Z., Liu, X., Tang, Q., Peng, X., Gao, B.Z.: Light field 3d measurement using unfocused plenoptic cameras. *Optics Letters* **43**(15), 3746–3749 (2018) [2](#), [3](#), [11](#), [12](#)
6. Cai, Z., Pedrini, G., Osten, W., Liu, X., Peng, X.: Single-shot structured-light-field three-dimensional imaging. *Optics Letters* **45**(12), 3256–3259 (2020) [2](#)
7. Heinze, C., Spyropoulos, S., Hussmann, S., Perwass, C.: Automated robust metric calibration of multi-focus plenoptic cameras. In: 2015 IEEE International Instrumentation and Measurement Technology Conference (I2MTC) Proceedings. pp. 2038–2043. IEEE (2015) [1](#), [5](#)
8. Heinze, C., Spyropoulos, S., Hussmann, S., Perwaß, C.: Automated robust metric calibration algorithm for multifocus plenoptic cameras. *IEEE Transactions on Instrumentation and Measurement* **65**(5), 1197–1205 (2016) [1](#)
9. Hog, M., Sabater, N., Vandame, B., Drazic, V.: An image rendering pipeline for focused plenoptic cameras. *IEEE Transactions on Computational Imaging* **3**(4), 811–821 (2017) [1](#)
10. Jeon, H.G., Park, J., Choe, G., Park, J., Bok, Y., Tai, Y.W., Kweon, I.S.: Depth from a light field image with learning-based matching costs. *IEEE transactions on Pattern Analysis and Machine Intelligence* **41**(2), 297–310 (2018) [1](#)
11. Johannsen, O., Heinze, C., Goldluecke, B., Perwaß, C.: On the calibration of focused plenoptic cameras. In: Time-of-Flight and Depth Imaging. Sensors, Algorithms, and Applications: Dagstuhl 2012 Seminar on Time-of-Flight Imaging and GCPR 2013 Workshop on Imaging New Modalities. pp. 302–317. Springer (2013) [1](#)
12. Kao, Y.H., Liang, C.K., Chang, L.W., Chen, H.H.: Depth detection of light field. In: 2007 IEEE International Conference on Acoustics, Speech and Signal Processing-ICASSP'07. vol. 1, pp. I–893. IEEE (2007) [1](#)
13. Liu, K., Wang, Y., Lau, D.L., Hao, Q., Hassebrook, L.G.: Dual-frequency pattern scheme for high-speed 3-d shape measurement. *Optics express* **18**(5), 5229–5244 (2010) [5](#)
14. Matoušek, M., Werner, T., Hlavác, V.: Accurate correspondences from epipolar plane images. In: Proc. Computer Vision Winter Workshop. pp. 181–189. Citeseer (2001) [1](#)
15. Moreno, D., Taubin, G.: Simple, accurate, and robust projector-camera calibration. In: 2012 Second International Conference on 3D Imaging, Modeling, Processing, Visualization & Transmission. pp. 464–471. IEEE (2012) [14](#)
16. Mousnier, A., Vural, E., Guillemot, C.: Partial light field tomographic reconstruction from a fixed-camera focal stack. *arXiv preprint arXiv:1503.01903* (2015) [1](#)
17. Ng, R., Levoy, M., Brédif, M., Duval, G., Horowitz, M., Hanrahan, P.: Light field photography with a hand-held plenoptic camera. Ph.D. thesis, Stanford university (2005) [2](#)
18. Park, I.K., Lee, K.M., et al.: Robust light field depth estimation using occlusion-noise aware data costs. *IEEE transactions on Pattern Analysis and Machine Intelligence* **40**(10), 2484–2497 (2017) [1](#)
19. Perwass, C., Wietzke, L.: Single lens 3d-camera with extended depth-of-field. In: Human vision and electronic imaging XVII. vol. 8291, pp. 45–59. SPIE (2012) [1](#), [3](#), [6](#)

20. Srinivasan, M.W.T.P.P., Rusinkiewicz, S.H.S., Ramamoorthi, J.M.R.: Shape estimation from shading, defocus, and correspondence using light-field angular coherence. *IEEE Transactions on Pattern Analysis and Machine Intelligence* **39**(3) (2017) [1](#)
21. Tao, M.W., Hadap, S., Malik, J., Ramamoorthi, R.: Depth from combining defocus and correspondence using light-field cameras. In: *Proceedings of the IEEE International Conference on Computer Vision (ICCV)*. pp. 673–680 (2013) [1](#)
22. Wang, T.C., Efros, A.A., Ramamoorthi, R.: Depth estimation with occlusion modeling using light-field cameras. *IEEE transactions on Pattern Analysis and Machine Intelligence* **38**(11), 2170–2181 (2016) [1](#)
23. Wanner, S., Fehr, J., Jähne, B.: Generating epi representations of 4d light fields with a single lens focused plenoptic camera. In: *Advances in Visual Computing: 7th International Symposium, ISVC 2011, Las Vegas, NV, USA, September 26–28, 2011. Proceedings, Part I* 7. pp. 90–101. Springer (2011) [1](#)
24. Wanner, S., Goldluecke, B.: Globally consistent depth labeling of 4d light fields. In: *Proceedings of IEEE Conference on Computer Vision and Pattern Recognition (CVPR)*. pp. 41–48. IEEE (2012) [1](#)
25. Wu, J., Liu, S., Wang, Z., Zhang, X., Guo, R.: Dynamic depth estimation of weakly textured objects based on light field speckle projection and adaptive step length of optical flow method. *Measurement* **214**, 112834 (2023) [2](#)
26. Yalla, V.G., Hassebrook, L.G.: Very high resolution 3d surface scanning using multi-frequency phase measuring profilometry. In: *Spaceborne Sensors II*. vol. 5798, pp. 44–53. SPIE (2005) [5](#), [8](#), [11](#)
27. Yu, Z., Guo, X., Lin, H., Lumsdaine, A., Yu, J.: Line assisted light field triangulation and stereo matching. In: *Proceedings of the IEEE International Conference on Computer Vision (ICCV)*. pp. 2792–2799 (2013) [1](#)
28. Zhang, G., Xu, B., Lau, D.L., Zhu, C., Liu, K.: Correcting projector lens distortion in real time with a scale-offset model for structured light illumination. *Optics Express* **30**(14), 24507–24522 (2022) [14](#)
29. Zhang, Y., Lv, H., Liu, Y., Wang, H., Wang, X., Huang, Q., Xiang, X., Dai, Q.: Light-field depth estimation via epipolar plane image analysis and locally linear embedding. *IEEE Transactions on Circuits and Systems for Video Technology* **27**(4), 739–747 (2016) [1](#)
30. Zhang, Z.: A flexible new technique for camera calibration. *IEEE Transactions on Pattern Analysis and Machine Intelligence* **22**(11), 1330–1334 (2000) [14](#)
31. Zhou, P., Wang, Y., Xu, Y., Cai, Z., Zuo, C.: Phase-unwrapping-free 3d reconstruction in structured light field system based on varied auxiliary point. *Opt. Express* **30**(17), 29957–29968 (Aug 2022) [2](#)